Optical System Design for Noncontact, Normal Incidence, THz Imaging of in vivo Human Cornea

Sung, Shijun; Dabironezare, Shahab; Llombart, Nuria; Selvin, Skyler; Bajwa, Neha; Chantra, Somporn; Nowroozi, Bryan; Garritano, James; Goell , Jacob; Li, Alex

DOI
10.1109/TTHZ.2017.2771754

Publication date
2018

Document Version
Accepted author manuscript

Published in
IEEE Transactions on Terahertz Science and Technology

Optical System Design for Noncontact, Normal Incidence, THz Imaging of *in vivo* Human Cornea

Shijun Sung, Shahab Dabironezare, Nuria Llombart, Skyler Selvin, Neha Bajwa, Somporn Chantra, Bryan Nowroozi, James Garritano, Jacob Goell, Alex Li, Sophie X. Deng, Elliott Brown, Warren S. Grundfest, and Zachary D. Taylor

***Abstract*—Reflection-mode terahertz (THz) imaging of corneal tissue water content (CTWC) is a proposed method for early accurate detection and study of corneal diseases. Despite promising results from *ex vivo* and *in vivo* cornea studies, interpretation of the reflectivity data is confounded by the contact between corneal tissue and dielectric windows used to flatten the imaging field. Herein, we present an optical design for noncontact THz imaging of cornea. A beam-scanning methodology performs angular normal incidence sweeps of a focused beam over the corneal surface while keeping the source, detector, and patient stationary. A quasi-optical analysis method is developed to analyze the theoretical resolution and imaging field intensity profile. These results are compared to the electric field distribution computed with a physical optics analysis code. Imaging experiments validate the optical theories behind the design and suggest that quasi-optical methods are sufficient for designing of THz corneal imaging systems. Successful imaging operations support the feasibility of noncontact *in vivo* imaging. We believe that this optical system design will enable the first, clinically relevant, *in vivo* exploration of CTWC using THz technology.**

***Index Terms*—Biological and medical imaging, clinical instruments, medical diagnostics, terahertz (THz) imaging of cornea.**

Manuscript received May 22, 2017; revised July 29, 2017; accepted September 29, 2017. Date of publication November 22, 2017; date of current version January 9, 2018. This work was supported in part by the National Eye Institute under Grant 5R01EY021590. *(Corresponding author: Shijun Sung.)*

S. Sung and S. Selvin are with the Department of Electrical Engineering, University of California, Los Angeles, CA 90095 USA (e-mail: junsung@ucla.edu; skyler.selvin@gmail.com).

S. Dabironezare and N. Llombart are with the Center for Wireless Systems and Technology, Delft University of Technology, 2628 CD Delft, The Netherlands (e-mail: S.O.Dabironezare-1@tudelft.nl; n.llombartjuan@tudelft.nl).

N. Bajwa, J. Garritano, J. Goell, and A. Li are with the Department of Bioengineering, University of California, Los Angeles, CA 90095 USA (e-mail: nbajwa1@gmail.com; jim.garritano@gmail.com; jhgoell@berkeley.edu; alexli711@gmail.com).

S. Chantra and S. X. Deng are with the Department of Ophthalmology, University of California, Los Angeles, CA 90095 USA (e-mail: chantrasomporn@yahoo.com; deng@jsei.ucla.edu).

B. Nowroozi was with the Department of Bioengineering, University of California, Los Angeles, CA 90095 USA. He is now with Mimeo Labs Inc., Santa Monica, CA 90404 USA (e-mail: bnowroozi@ucla.edu).

E. Brown is with the Department of Electrical Engineering, Wright State University, Dayton, OH 45435 USA (e-mail: elliott.brown@wright.edu).

W. S. Grundfest and Z. D. Taylor are with the Department of Electrical Engineering and the Department of Bioengineering, University of California, Los Angeles, CA 90095 USA (e-mail: warrenbe@seas.ucla.edu; zdeis@seas.ucla.edu).

Color versions of one or more of the figures in this paper are available online at http://ieeexplore.ieee.org.

I. Introduction

CORNEAL disorders, such as Fuchs' endothelial dystrophy [1], keratoconus [2], pseudophakic bullous keratopathy, and graft rejection [3], [4], are characterized by increased corneal tissue water content (CTWC) and subsequent swelling of the cornea, leading to chronic vision impairment and often requiring surgical intervention. Corneal disorders affect large populations worldwide especially that of elderly [5]. It is believed that abnormal CTWC is a key clinical manifestation of endothelial malfunctions and corneal dystrophies [6]–[10]. Because abnormal CTWC is an important diagnostic target for assessing the extent of tissue damage *in vivo* [6]–[10], quantifying and tracking CTWC can 1) provide a better understanding of the formation, development, and progression of these disorders; and 2) become a clinically useful method for early diagnosis and assist in the choice and timing of interventions. However, accurate and noninvasive *in vivo* measurement of CTWC remains elusive.

Terahertz (THz) imaging is a promising method for the sensing and imaging of CTWC due to the homogeneity of bulk corneal tissue and relative lack in physiologic variations in corneal topography compared to other structures in the body. However, despite the acquisition of clinically relevant data from *ex vivo* and *in vivo* cornea, interpretation of the results has been confounded by contact between cornea and field-flattening dielectric windows that are required in standard flat-field THz imaging methods [11], [12].

In this work, we describe reflective THz imaging optical principles that use a combination of planar and off-axis parabolic (OAP) mirrors to scan a beam at the normal incidence across the surface of cornea while keeping the source, detector, and patient stationary. This method acquires an image of a spherical surface with an arbitrary radius of curvature by an orthographic projection of the spherical surface to Cartesian coordinates. The design enables noncontact imaging of corneal reflectivity and avoids deformations of the cornea, which was a critical confounder in our previous work [11], [12].

The following sections introduce the design and simulation of scanning optics for noncontact CTWC imaging of human cornea. Imaging principles, quasi-optical modeling, and physical optics modeling are presented. The quasi-optical modeling treats the OAP mirror as an ensemble of thin lenses of varying effective focal lengths (EFLs). The accuracy of this quasi-optical

technique is assessed with a physical optics simulation code. A prototype imaging system is presented and was used to evaluate the utility of the presented optical simulations

II. Motivation for Current Work

In previous studies [11]–[13], we investigated the utility of THz and millimeter wave imaging and sensing to track changes in CTWC. A rabbit model study ($n = 5$) was designed to mimic disease-relevant CTWC perturbations. A dehydration protocol was applied to one cornea of each animal, and the subsequent expected rehydration was observed over a 90-min period. During this time window, central corneal thickness (CCT) measurements were acquired with an ultrasound pachymeter (current clinical standard), and the corresponding THz reflectivities were acquired with a 100-GHz (narrowband) reflectometer and ∼525-GHz (broadband) imaging system. The protocol included the application of a 12-μm-thick Mylar window to gently flatten the cornea and provide a planar surface for both systems.

The experiment revealed a strong positive correlation between increasing CCT and increasing 100-GHz reflectivity, both consistent with the intended increase in CTWC. However, the 525-GHz imaging data did not demonstrate a statistically significant increase or decrease in reflectivity and produced a limited correlation with the millimeter wave and the CCT measurement [11], [12]. An electromagnetic modeling of this problem indicated that *in vivo* cornea is a lossy etalon at millimeter wave and THz frequencies, and thus, its spectral properties are a complex coupling of CTWC and CCT [11], [12]. Model-based analysis suggested that the protocol most likely modified the thickness of the cornea while leaving the aggregate CTWC relatively unperturbed, thus resulting in a resolvable "etalon effect" at 100 GHz and an apparent absence of etalon at 525 GHz. It is likely that the contact pressure of the window altered the CCT, while the stream of air produced negligible variation in CTWC.

These experiments confirmed weaknesses in the exploration of THz imaging for CWTC diagnostics with current techniques. First, active imaging of the corneal surface is difficult with simple *xy* scanning techniques. The corneal surface is only ∼10 mm in diameter *en face* and nearly spherical with a mean radius of curvature of ∼8 mm [14]. This geometry constrains measurements to the central apex of the cornea when using conventional planar raster scanning [11]. Second, all current clinically accepted techniques of determining CTWC *in vivo* are based on thickness measurements that extrapolate CTWC from CCT [15]. Application of a dielectric field-flattening window confounds CCT-to-CTWC mapping and perturb measured THz reflectivity. Considering these shortfalls, it is apparent that THz imaging of CTWC requires an improved THz imaging method that can acquire reflectivity maps of the cornea *in vivo* without contact.

To address these needs, we have designed, constructed, and characterized a system that acquires reflectivity maps of the cornea without contact. The system architecture was motivated by two key observations: 1) The cornea is nearly a perfect hypo hemisphere with respect to a THz wavelength and the person-to-person variations of corneal curvature are relatively small; and 2) the *en face* diameter of the cornea is also relatively

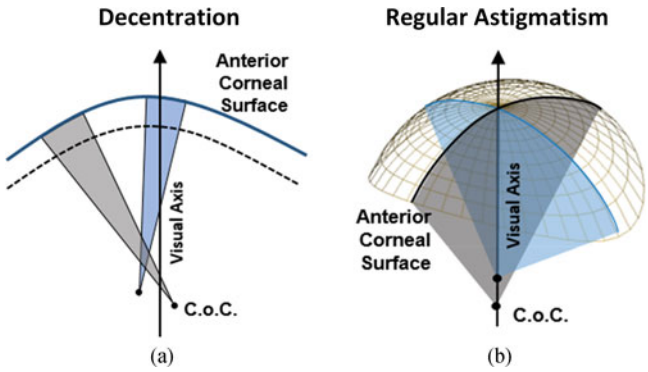

Fig. 1. Corneal anatomy. The anterior and posterior surfaces are represented by the curved solid and dotted lines, respectively. (a) Decentration: local surfaces may have CoC that do not lie on the central optical axis. (b) Astigmatism: Radial asymmetry results and focal points from different axes lying at different depths along the optical axis.

consistent across the adult population. The target curvature and field of view (FOV) can be assumed *a priori* with a high degree of confidence. Therefore, corneal imaging is unique among all THz medical imaging applications and allows the system design to accommodate only a very limited set of use cases.

III. Spherical Properties of the Cornea

The anterior cornea (surface) is aspherical where the deviation from an ideal sphere increases toward the periphery [16]. Human cornea is also astigmatic, demonstrating different curvature and, hence, optical power as a function of cross-sectional meridian angles [17]. Characterization of corneal topology is important for interventions such as laser-assisted in situ keratomileusis and photorefractive keratectomy. Topological maps can be obtained with videokeratography [18] or Scheimpflug photography [19] techniques, which interpret the surface height measurements in refractive power at each local surface. In particular, videokeratography [20] can be used to construct dioptric power maps from corneal surface height data, which can be further fitted to a parametric surface to analyze higher order surface features from disease or refractive surgery [21]. However, despite the maturity of topology mapping technology, there is no standardized method for analyzing topographic information [22]. Therefore, the following analysis is performed to characterize physiologic variations of anterior corneal surface.

Corneal surface data are decomposed into a set of concentric rings centered at the corneal apex. Fourier decomposition analysis was utilized to explore the deviations between average human cornea topology and an ideal sphere [22], [23]. The fundamental mode (the first term in the Fourier series expansion) is attributed to decentration [see Fig. 1(a)], and the second term is attributed to "regular" astigmatism [see Fig. 1(b)]. The RoC deviation data in Fig. 2 represent the expected geometric variation from an ideal sphere. Higher order Fourier terms are grouped together as "higher order surface irregularities" and are shown to contribute much less to the overall corneal shape than either decentration or astigmatism individually. In general, the Fourier coefficients increase for equal height contour lines further from the corneal apex.

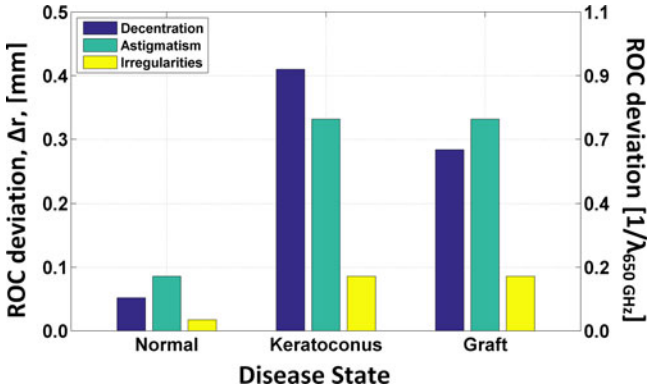

Fig. 2. Average corneal RoC variation [Δr, (1)] for healthy cornea (left), keratoconus (middle), and grafted cornea (right). The contribution to overall RoC variation is decomposed into decentration, regular astigmatism, and higher order irregularities [22]. The maximum RoC variation is less than 1λ @ 650 GHz.

In [22], corneal surface curvature measurements are reported as diopters (D) across the meridian cross section as a function of radial distance from the center of the cornea and the meridian angle. The diopter values are averaged and converted to an expected RoC deviation using (1), where P_{typical} is the focusing power of a cornea representative of typical population ($P_{\text{typical}} = 44\text{D}$), P_{measured} is the data from [22], n is the refractive index of the cornea ($n = 1.376$), and $\Delta \boldsymbol{r}$ is the resulting standard deviation in the RoC:

$$\Delta r = (n-1)\left(\frac{1}{P_{\text{measured}}} - \frac{1}{P_{\text{typical}}}\right) \qquad (1)$$

The average RoC deviation from the first term in the series (decentration), the second term in the series (astigmatism), and the higher order terms is displayed in Fig. 2 for healthy eyes ($N=25$), keratoconic eyes ($N=13$), and grafted cornea ($N=20$) [22]. The format represents the expected geometric variation from an ideal sphere. Data for endothelial dystrophies, such as Fuchs, were not available during the preparation of this manuscript. However, the expected deviation arising from dystrophies is expected to much less that keratoconus; thus, the pathologies in Fig. 2 serve as sufficient upper bound.

For normal healthy eyes, decentration produces a mean RoC displacement deviation of ~0.05 mm, regular astigmatism is slightly higher at ~0.08 mm, and the sum total of higher modes contributes a negligible ~0.015 mm. Keratoconus, a condition where the cornea thickens and the CCT increases at a rate faster than the periphery [2], [24], [25], exhibits mean RoC displacement deviations up to ~0.4 mm. Finally, for grafted cornea, where a patient's diseased cornea has been removed and replaced with a donor cornea [4], the mean RoC displacement deviation arising for decentration, astigmatism, and higher order irregularities is ~0.3, ~0.35, and ~0.08 mm, respectively.

It is instructive to view this RoC curvature variation with respect to a free-space wavelength of 0.462 mm (650 GHz), the center wavelength of the system in Section VIII (cf. Fig. 10). When normalized to illumination wavelength, the corneal radius of curvature is ~8 mm/0.462 mm = 17.32λ. Assume that the variations described by the decentration, astigmatism, and

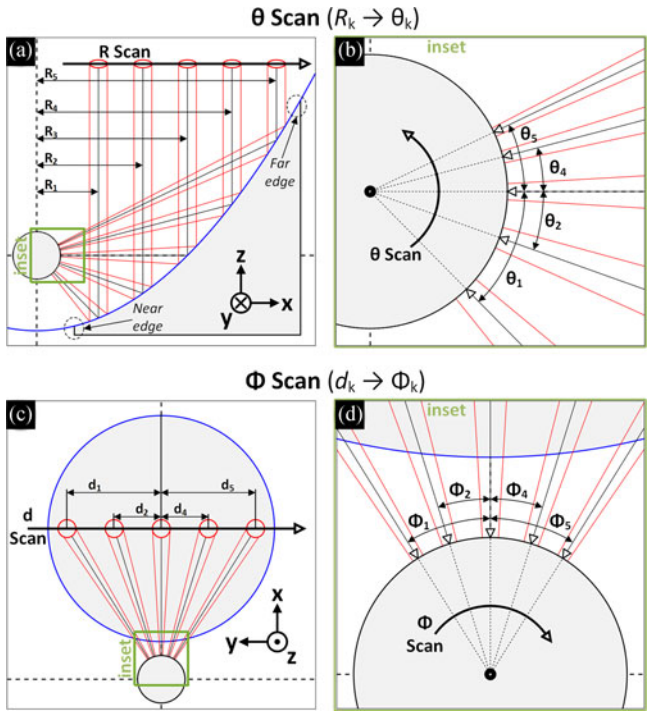

Fig. 3. Mapping of transverse translation in the mirror CA plane to angular translation on the corneal surface. In (a) and (b), transverse locations $R_1 - R_5$ are mapped to angular scan locations $\theta_1 - \theta_5$. In (c) and (d), transverse scan locations $d_1 - d_5$ are mapped to angular scan locations $\phi_1 - \phi_5$. Note that the focused beam is intercepted prior to the focal point and that all beams are normal to the corneal surface.

higher order irregularities are uncorrelated, and that the total standard deviation can be computed as the square root of the sum of squares of each individual standard deviation. Then, the resulting RoC variations are the following: normal healthy cornea = 17.32λ ± 0.21λ, keratoconus = 17.32λ ± 1.16λ, and grafted cornea = 17.32λ ± 1.01λ, corresponding to coefficients of variance ($100*\sigma/\mu$) of 1.21%, 6.69%, and 5.83%, respectively. Hence, with respect to the 650-GHz illumination, the corneal surface can be considered an ideal sphere with maximum expected deviations approximately one free-space wavelength.

IV. Spherical Surface Imaging

A. Spherical Surface Scanning Principle

Imaging of a spherical surface is performed by positioning the centers of curvature (CoC) of the target (cornea) coincident with the focal point of an OAP mirror and then transmitting a collimated illumination beam into the mirror clear aperture (CA), parallel to the CA normal (see Fig. 3).

The focused radiation is normal to the spherical surface and, in the limit of geometric optics, has a phase front curvature equal to the spherical surface RoC. The reflected diverging beam is recollimated by the OAP mirror and arrives coincident with the transmitted beam path. Modulating the transverse location of the collimated beam while maintaining a path parallel to the plane of mirror's CA sweeps the location of the illumination spot on the spherical surface, and an image can be constructed

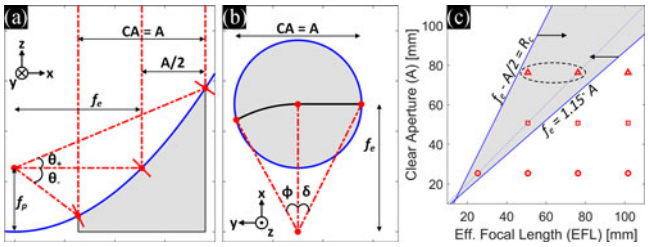

Fig. 4. Half angles of 90° OAP mirrors: ϕ, δ, θ_+, and θ_-. (a) Side view. (b) CA view. (c) Design space bordered by offset $f_e - \mathrm{A}/2 = R_c$ and $f_e = 1.15$ A. Standard commercially available mirrors indicated by [○] 25.4-mm, [□] 50.8-mm, and [Δ] 76.2-mm apertures.

TABLE I
SPHERICAL SCANNING ANGLES (IN DEGREES) BY AN IMAGING REFLECTOR $f/\#$

$f/\#$ (f_e/A)	0.66	1	2	3
θ_-	62.8	36.9	16.3	10.4
θ_+	30.7	22.6	12.7	8.8
ϕ	44.5	29.0	14.4	9.6
δ	37.2	26.6	14.0	9.5

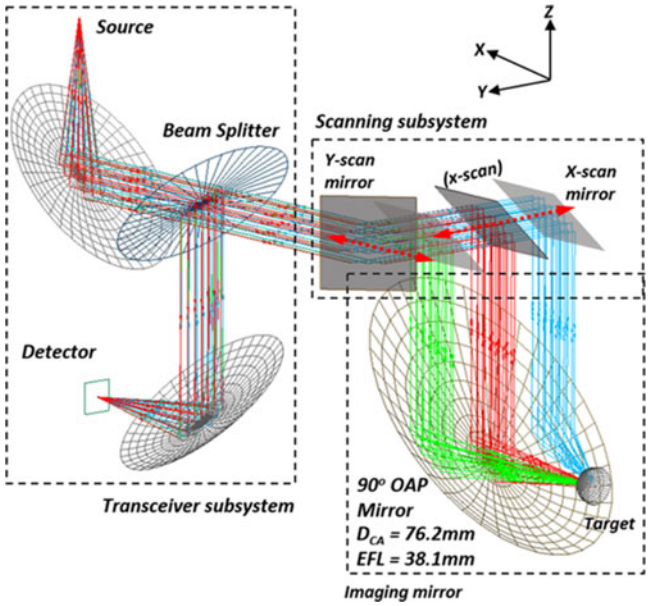

Fig. 5. Imaging system design. The raypath is plotted starting from the source, then traced to the scanning mirrors (only *x*-scanning shown), target, and back to the detector. If the target is spherical, all rays focus to a point on the detector, invariant to scan mirror position.

(see Fig. 3). The retrodirective nature of this arrangement is compatible with any transceiver design that can multiplex/demultiplex the input and output beams using, e.g., a wire grid, thin film, or polarizing beam splitter.

This beam-scanning technique accomplishes spherical surface (θ,ϕ) scanning by the geometrical projection of the target's spherical surface into the planar coordinate system (x,y) in the mirror CA. This is a restatement of the Fourier transform property of an optical focusing element as demonstrated with a 90° OAP mirror in Fig. 3, where transverse locations R_k and d_k are mapped to angular locations θ_k and ϕ_k, respectively. Unlike the Mercator projection that transforms the surface from spherical coordinates via a cylindrical projection to rectilinear coordinates [26], this method performs conformal mapping from spherical coordinates via projection by a paraboloid surface into a rectilinear coordinate system. Although this exact mapping operation is uncommon, it shares resemblance to the conic orthographic mapping projections in cartography, such as the Lambert conformal conic projection [27].

B. Effective Imaging Optic *f*/# and Offset

The mirror scanning solid angle can be characterized by the mirror $f/\# = f_e/A = 2f_0/A$, where f_e is the EFL, f_0 is the parent focal length (PFL, $f_e = 2f_0$ for a 90° OAP), and A is the CA diameter [see Fig. 4(a)]. A human cornea spans $\sim$60° ($\pm$30°) about its apex; thus, an imaging optic should approach $f_e/A = 2 \cdot \tan(30^\circ) \sim 1.15$ to span $\pm$30° in both azimuthal [see Fig. 3(c)] and elevation [see Fig. 3(a)] about the corneal apex.

Table I lists the azimuthal and elevation angles subtended by a 90° OAP reflector, according to commonly available *f*/#s from vendors. Because the focusing geometry (see Fig. 4) is asymmetric, the azimuthal coverage angle ($\theta_- + \theta_+$) [see Fig. 4(a)] is not bisected by the 90° ray (i.e., $\theta_- > \theta_+, \forall f_e, A$). The 90° geometry results in the relation $\theta_+ < \delta < \phi < \theta_-$; therefore, θ_+ forms the lower bound on the OAP *f*/#. The results in Table I and Fig. 4 that a 25.4-mm PFL, 76.2-mm CA OAP (2·25.4/76.2 = *f*/0.66) mirror can scan the entire angular extent of the cornea.

f/# is scale invariant and does not consider the size of the target relative to the size of the focusing objective. Practical considerations restrict combinations of focal length and CA to pairs that avoids positioning the apex of the cornea inside the mirror. In other words, the "flange distance" should be greater than the corneal radius of curvature: $f_e - A/2 > R_c$. The flange distance and *f*/# are displayed in Fig. 4(c), where all combinations to the right of the $f_e - A/2 = R_c$ line yield sufficiently large offsets and all combinations to the left of the $f_e = 1.15$ A yield *f*/#s sufficient angular coverage. Markers representing standard, commercially available pairs of EFLs and apertures are superimposed on this space with the 76.2-mm-diameter mirrors indicated by the dotted contour. This work utilized a 76.2-mm-diameter *f*/0.66 OAP.

V. QUASI-OPTICAL ANALYSIS

A method to implement the beam scanning described in Fig. 3 utilizes a set of plane mirrors, labeled x-scan and y-scan, that translate a collimated input beam in two orthogonal directions parallel to the CA plane of the OAP mirror. This concept is displayed in Fig. 5, where the input and output beams are multiplexed/demultiplexed by a beam splitter that optically collocates the source and detector.

The optics are laid out in three groups, which transmit and receive collimated beams: transceiver subsystem, scanning subsystem, and imaging mirror. The corneal CoC is coincident with the OAP mirror's focal point, and all rays of the focused beam

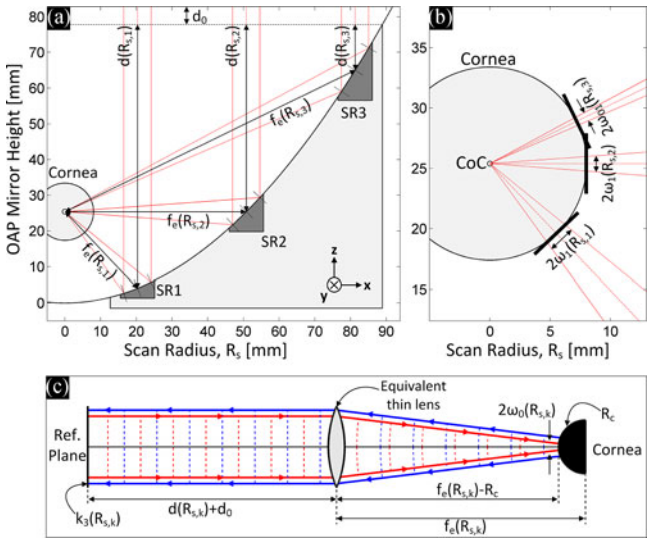

Fig. 6. Raypath diagram of the beam scanning. (a) Parabolic mirror segmentation location. (b) Definition of reference plane tangent to the corneal surface at the intersection of beam centroid and cornea. The focused spot size was characterized on these reference planes. This is where spot size on the surface of the cornea. (c) Thin lens equivalent of the overall beam path.

are orthogonal to the spherical surface. Thus, all reflected rays, independent of scan mirror position, will arrive at the detector feedhorn with identical convergence angle, transverse location, and extent as demonstrated with the three-superimposed beam paths in Fig. 5 (ASAP, Breault Inc.).

A. Quasi-Optical Analysis Setup and Modeling

The imaging mirror in Fig. 5 is much larger than the transverse extent of the collimated input beam ($A >> \omega_0$). At any scan location, the beam only sees a local surface of the imaging OAP mirror, from here on referred to as subreflector. Therefore, the transformation of the THz beam as a function of scan location can be approximated as the transformation by an optic whose properties represent the subreflector, mirror surface subtended by the beam waist. Given a reasonable input collimated beam size, the segments span moderate changes in curvature and focal distance and substantially reduced asymmetry about the beam centroid. These points suggest that the subreflector can be accurately modeled as a thin lens whose focal length is equal to the central beam path length from the mirror surface to the focus. This setup enables the use of quasi-optical analysis with Gaussian optics and ABCD matrices to compute the resulting beam transformations as a function of scan location and, thus, the image transfer function of the imaging OAP mirror [28].

The Gaussian beam setup is displayed in Fig. 6(a), where the shaded areas represent the cross sections of a cornea (8-mm RoC) and a 76.2-mm CA, 25.4-mm PFL, 90º OAP mirror. Three parallel ray bundles are normal to the CA plane, and the corresponding subreflectors are represented by the darker shaded areas. A Gaussian beam can be traced through each subreflector using: 1) the distance of free-space travel between a reference plane and the mirror surface height defined by the intersection of the parabolic profile and collimated beam centroid, and 2) the EFL of the subreflector defined by the line segment connecting the intersection in 1) and the effective focal point of the parent OAP mirror. This concept yields a collimated path length, a focused path length, and an EFL that are all dependent on the lateral distance (R_s) between the mirror focal point and collimated beam centroid [horizontal axis in Fig. 6(a)]. The problem is recast to that described by Fig. 6(c). To complete the problem description, a reference plane is defined at a distance d_0 from the upper tip of the OAP represented by the dotted line in Fig. 6(a). This reference plane is where the collimated beam (plane coincident with the beam waist) was launched. The collimated beam travels a distance $d(R_s) + d_0$, is focused by a thin lens of $f_e(R_s)$, and then travels $f_e(R_s) - R_c$ to a convex reflector of radius R_c (cornea). The mirror and corneal geometry ensure normal incidence for all R_s within the CA of the mirror, resulting in the beam retracing its path back through the mirror collinear with the incidence path as follows:

$$f_e\ (R_s) = (4f_0)^{-1}\ {R_s}^2 + f_0 = f_e \tag{2}$$

$$d\ (R_s) = (4f_0)^{-1}\ \left[\left(2f_p + \frac{A}{2}\right)^2 - R_s^2\right] = d. \tag{3}$$

Expressions for the radially dependent focal length and beam CA path length are defined in (2) and (3). Note that these expressions are defined for the domain $R_s\ \epsilon\ 2f_0 \pm A/2$ and are explicitly for a 90º OAP as

$$M_{P\to C}\ (R_m) = \begin{bmatrix} 1 & f_e - R_C \\ 0 & 1 \end{bmatrix} \begin{bmatrix} 1 & 0 \\ -f_e^{-1} & 1 \end{bmatrix} \begin{bmatrix} 1 & d + d_0 \\ 0 & 1 \end{bmatrix} \tag{4}$$

$$M_{C\to P}\ (R_m) = \begin{bmatrix} 1 & d + d_0 \\ 0 & 1 \end{bmatrix} \begin{bmatrix} 1 & 0 \\ -f_e^{-1} & 1 \end{bmatrix} \begin{bmatrix} 1 & f_e - R_C \\ 0 & 1 \end{bmatrix} \tag{5}$$

$$M_C = \begin{bmatrix} 1 & 0 \\ 2/R_C & 1 \end{bmatrix} \tag{6}$$

$$\boldsymbol{M_1} = M_{P\to C} \tag{7}$$

$$\boldsymbol{M_2} = M_C\ M_{P\to C} = M_C\ \boldsymbol{M_1} \tag{8}$$

$$\boldsymbol{M_3} = M_{C\to P}\ M_C\ M_{P\to C} = M_{C\to P}\ \boldsymbol{M_2}. \tag{9}$$

$\boldsymbol{M}_1 = M_{P\to C}$ [see (4) and (7)] is the transfer matrix describing the propagation of the beam from the reference plane (P) to the cornea (C). $\boldsymbol{M}_2 = M_C\ M_{P\to C}$ [see (6) and (8)] describes the transformation of the beam by $\boldsymbol{M}_1$ and the subsequent reflection from the spherical reflector. The overall retrodirective transmission through the optical system is described by $\boldsymbol{M}_3 = M_{C\to P}\ M_C M_{P\to C}$ [see (6) and (9)], where the beam starts and stops at the reference plane:

$$\frac{1}{q_k} = \frac{1}{R_k} - j\frac{\lambda_0}{\pi n \omega_k^2} \quad \to \quad \frac{1}{q_0} = -j\frac{\lambda_0}{\pi n \omega_k^2} \tag{10}$$

$$\boldsymbol{M_k} = \begin{bmatrix} A_k & B_k \\ C_k & D_k \end{bmatrix} \tag{11}$$

$$q_k = \frac{A_k q_0 + B_k}{C_k q_0 + D_k}. \tag{12}$$

The standard complex beam parameter relations listed in (10)–(12) were used to compute the spot size on target $(\boldsymbol{M}_1)$, the beam radius of curvature immediately prior to $(\boldsymbol{M}_1)$ and following $(\boldsymbol{M}_2)$ reflection from the cornea, and the coupling coefficient between the input and output beams at the reference plane $(\boldsymbol{M}_3)$. These metrics were calculated for all relevant R_s with input complex beam parameter q_0 parameterized by ω_0 and a constant $R_0 \rightarrow \infty$.

B. Spot Radius on the Corneal Surface

The spot size on the cornea was explored as a function of input beam waist size at the reference plane and the input collimated beam location described by its radial distance (R_s) from the focal point of the OAP mirror using (7), (10)–(12), and

$$\omega_1 = \frac{\lambda}{\pi}\left[\mathbb{R}\quad \frac{j}{q_1}\right\}\Bigg]^{-1}. \tag{13}$$

These equations characterize the spot size on a plane tangent to the corneal surface and normal to the beam centroid as depicted in Fig. 6(b). Due the relatively small extent of the focused beam with respect to the corneal RoC, the spot size computed on a plane was considered a close representation of projecting the beam on to the corneal surface and assessing the extent of the intersection contour.

The input Gaussian beam radius (ω_0) at the reference plane was varied from 4 to 12 mm, and the resulting output spot radius as a function of input radius and mirror scan radius (R_s) are superimposed on the shaded outline profile of a 76.2-mm CA, 25.4-mm PFL, 90° OAP mirror length for reference. Note the dotted line style at the extreme ends of each curve. The exterior points on both ends of the curves represent the edge of the mirror CA. The interior points, located closer to the mirror axis, represent one input beam radius (ω_0) from the edge of the mirror. In practice, diffractive effects may lead to a divergence between quasi-optical analysis and realized performance for beam centroid locations outside the solid line intervals.

The 4-mm input spot size demonstrates a decreasing focused spot size ω_1 for decreasing scam radius from $R_s = 85.05$ mm down to $R_s = 35.02$ mm corresponding to a beam radii of 3.36 and 1.96 mm, respectively. The focused beam radii then increase monotonically to 2.09 mm at the near edge of the mirror ($R_s = 15.78$ mm). For small-radius input beams, the combination of the subreflector focal length and center wavelength results in a beam waist that occurs "outside" of the cornea for large R_s; thus, the beam is diverging prior to incidence on the corneal surface. As the beam *f*/# is decreased (decreasing R_s) and the focused path length decreases (decreasing R_s), the beam waist decreases and its location converges to the surface of the cornea. Further decreases in R_s move the beam waist to "inside" the cornea and are concomitant with an increasing convergence angle. While the focused waist continues to decrease in size, the corneal surface intercepts the beam at a distance that is increasing from the location of the waist.

This behavior is somewhat reversed for the 12-mm input radius. The spot size on the corneal surface reaches its maximum at the shortest scan radius (shortest EFL), $R_s = 24.25$ mm, $\omega_1 = 3.1$ mm, and its minimum at the largest scan radius, $R_s = 76.58$ mm, $\omega_1 = 1.5$ mm. Unlike the 4-mm input beam, the 12-mm input beam produces a waist that is "inside" the cornea for all R_s, and the offset between the subreflector focal point and waist location is small with respect to the radius of the cornea (R_c) for nearly all R_s. Since the input beam is large, the effective beam *f*/# is small and leads to large convergence angles and thus large spot sizes on the corneal surface which is located a large number of Rayleigh lengths from the focal point (i.e., 8 mm $>> z_R$).

The intermediate input spot sizes demonstrate varying dependencies on the aforementioned factors, and it is clear by inspection of Fig. 7(a) that an intermediary balances the following three competing factors.

1) Decreasing R_s decreases the EFL of the subreflector and, thus, decreases the size of the focused beam waist.
2) Decreasing R_s increases the convergence angle of the beam and can increase the beam spot size on the corneal surface depending on beam input parameters.
3) Decreasing the input beam waist decreases the convergence angle while increasing the offset between subreflector focal point (corneal center of curvature) and focused beam waist. This can result in an increase or decrease in the spot size on the corneal surface depending on the *f*/# of the OAP, the input diameter of the beam, and the wavelength.

The results in Fig. 7 demonstrate a tradeoff relationship between input (ω_0) and focused (ω_1) beam radii and scan radius (R_s), which arises from characterizing the focused beam at a distance $R_c > 0$ from the geometric focal point, a factor unique to corneal imaging.

C. Beam Coupling Efficiency

The 2-D beam coupling coefficient beam is defined in

$$K_3\ (q_0, q_3) = \frac{4}{\left(\frac{\omega_0}{\omega_3} + \frac{\omega_3}{\omega_0}\right)^2 + \left(\frac{\pi\omega_0\omega_3}{\lambda}\right)^2 \left(\frac{1}{R_3} - \frac{1}{R_0}\right)^2}. \tag{14}$$

where the relationship between q_0 and q_3 is defined in

$$q_3 = \frac{A_3 q_0 + B_3}{C_3 q_0 + D_3} \tag{15}$$

and constructed with $\boldsymbol{M}_3$ from (9). The coupling coefficient was calculated at the reference plane and is written explicitly in terms of the input and output spot sizes and radii of curvature, which together define their respective complex beam parameters. Note that (14) assumes infinite reflector transverse extent and does not account for diffraction.

The coupling coefficient as a function of mirror position and input beam diameter is displayed in Fig. 7(b), which demonstrates the expected relation between input and output beam matching. As the beam input radius increases and the subreflector EFL decreases (decreasing R_s), the RoC matching between the focused beam and cornea improves, resulting in a reduced perturbation of the illumination beam and increased matching at the reference plane. The 12-mm beam ranges from 0.57 to 0.95 and the 4-mm beam ranges from 0.30 to 0.03. These results confirm a monotonically decreasing coupling

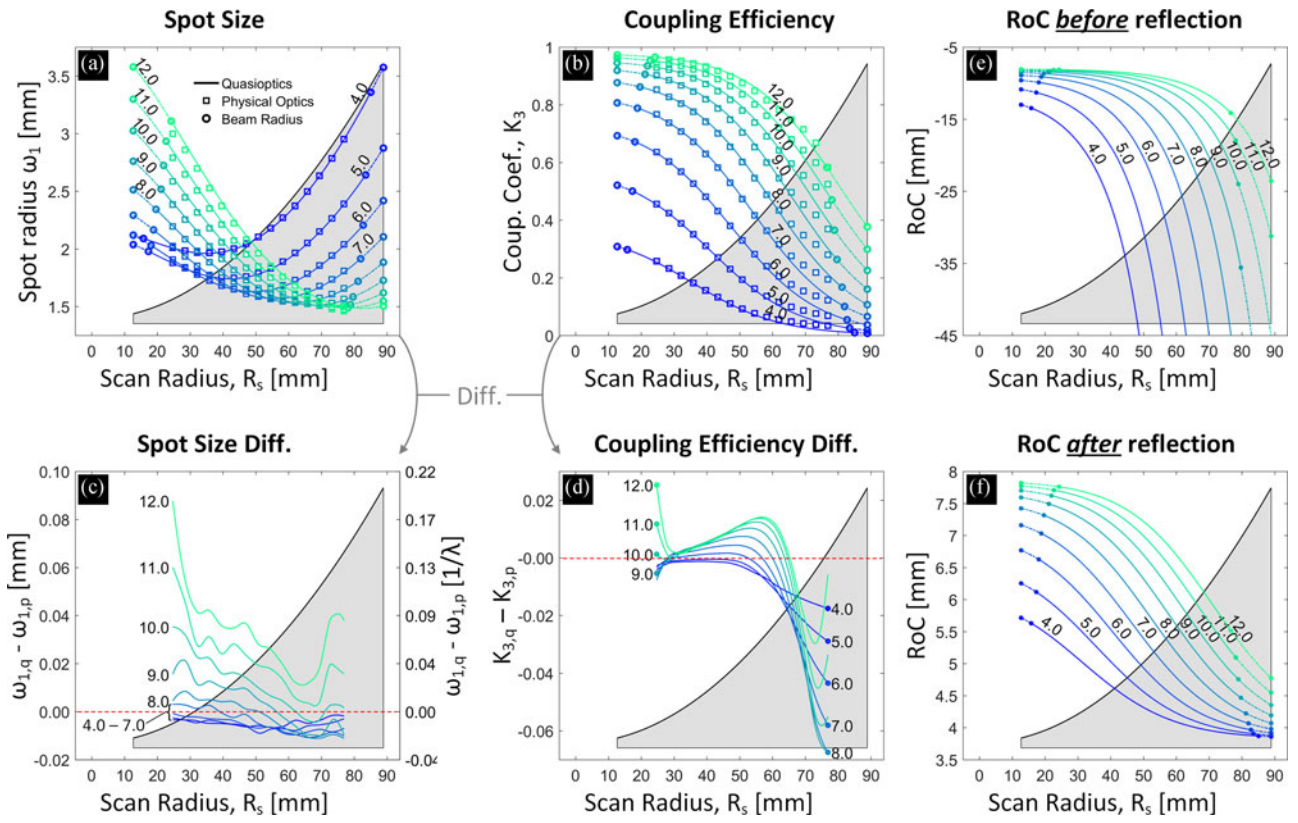

Fig. 7. Quasi-optical and physical optics computations of relevant beam parameters. The physical optics results are discussed in Section VI. (a) Focused spot radius on the analysis plane [see Fig. 6(b)] as a function of the input beam location (R_s) over the parabolic profile of the imaging OAP mirror. Each curve represents different collimated beam radii (ω_0) ranging from 4 to 12 mm. A scaled overlay of parabolic cross section is shown to depict the location of the beam. (b) Coupling coefficient between the input and output beam as a function of input beam location over the parabolic profile of the imaging OAP mirror. (c) Differential between quasi-optics and physical optics computations for ω_1. (d) Differential between quasi-optics and physical optics computations for K_3. Radius of curvature of the beam immediately on the target surface (e) and immediately after reflection (f), as a function of the input beam radial location over the parabolic profile of the imaging OAP mirror. Strong agreement was observed between the quasi-optical analysis and physical optics computations. Maximum deviation occurs for larger input diameters near the edge of the mirror indicating diffraction.

efficiency for increasing input radius, independent of the input beam radius

The source and detector mirrors in Fig. 5 were oriented, with respect to the beam splitter, to maintain an "ortho" configuration [29], [30]. Similarly, the beam bath through the focused mirror was retrodirective; thus, its beam transformation can be described as the output of two identical OAP mirrors also oriented in the "orthro" configuration. Finally, the beam patterns of the source and detector were considered identical to reflect the 26-dB feedhorns used in Section VIII. Due to the optical system symmetry, the similarly of the transmitted and received beams at the beam splitter (reference plane) was deemed a sufficient estimate of the coupling efficiency between the detector pattern and the transformed source pattern.

D. Beam RoC and Coupling

The RoCs for pre (R_1) and post (R_2) corneal reflection are displayed in Fig. 7(e) and (f), respectively, and were computed with

$$R_{1,2} = \left[\mathbb{R}\quad \frac{1}{q_{1,2}}\right\}\right]^{-1}. \tag{16}$$

The prereflection RoCs are consistent with the observed behavior in the spot size characterization shown in Fig. 7(a).

The RoCs resulting from the smaller input spot sizes are asymptotic and rapidly diverge to $-\infty$ for larger mirror R_s and then should approach, from $+\infty, +1/R_s$. Note that in Fig. 7(e), only the negative RoCs are plotted and asymptotes/asymptotic behavior were omitted for clarity. As the input spot size is increased, the beam waist decreases and its location converges to the corneal CoC. While most of the focused beam RoCs appear to be asymptotic, only the RoCs computed from the 4-, 5-, and 6-mm beams flip sign. These occur at $R_s = 68.17$ mm, $R_s = 75.68$ mm, and $R_s = 82.26$ mm for the $\omega_0 = 4$ mm, $\omega_0 = 5$ mm, and $\omega_0 = 6$ mm, respectively. All other considered beam radii maintain focused waist location "inside the cornea" for all R_s.

The reflected beam RoC demonstrates significantly less variation than the prereflection RoC as a function of mirror radius R_s and exhibits positive radii (divergence) for all input beam radii and mirror scan locations. Furthermore, the high empirical correlation of the trends with the computed coupling coefficients suggests that the postreflection RoC is the primary determinant of the coupling efficiency in the presented optics configuration.

E. Observations

The quasi-optical design and analysis space for corneal imaging is unique because 1) the target is spherical, leading to increased divergence in reflection compared to the canonical flat target; and 2) the target surface is NOT located at the focal point defined by the optics or beam calculations, leading to complex beam dynamics on target.

The results suggest that for a fixed input beam radius, and optimal alignment, the signal from the near edge (small R_s) of the mirror will always be higher than the far edge of the mirror (large R_s). These observations also suggest that the imaging field may be homogenized in terms of beam radius and coupling efficiency if the input beam radius is allowed to vary as a function of R_s. Finally, the results indicate that the minimum spot size on target does not coincide with the colocation of beam waist and corneal surface for the range of parameters examined.

Note that the analysis method used in this section can be extended to remove thin lens approximation treatment of the mirror surface segment. Any propagated beam can be decomposed to include higher order Hermite–Gaussian or Laguerre–Gaussian modes, and an augmented ray-transfer method can be applied to beam propagation, thereby accounting for the asymmetric geometry of the mirror segment [31]–[33].

VI. Physical Optics Analysis

The quasi-optical analysis of beam propagation was compared to computations by GRASP (Ticra Inc., Copenhagen, Denmark), a physical optics code typically used in reflector antenna design [34]–[36]. The cornea was modeled as dielectric half sphere with a refractive index of $n = 1.376$ and a radius of 8 mm. The quasi-optical system along with the sphere is simulated by a Gaussian beam source polarized along x. The source is located at the input beam plane with a vertical distance of 74.6 mm above the center of the sphere.

A. Spot Size

The focused electric field distribution was sampled in a transverse/tangent plane, located at the intersection of the beam centroid and corneal surface, for every input collimated beam radius (ω_0) and location (R_s) evaluated in Fig. 7. These planes are described by the x'- and z'-axes in Fig. 8(a) and (f) and are defined by the rotation of the reference frame (xyz) about the y-axis. The input beam was TM polarized (E-field aligned with the xz or $x'z'$ planes) to match the source in Section VIII.

An example of the focused beam for the input parameters $\omega_0 = 4$ mm and $R_s = 76.9$ mm is displayed in Fig. 8(a)–(c) in decibel scale with accompanying scale bars indicating FOV dimensions. The E-field distribution in the $x'z'$ plane confirms that the focused fields are nearly Gaussian. This distribution shape was also observed on the tangent target plane ($y'z'$), which demonstrates vanishingly small radial asymmetry (ellipticity $\sim$1) and an apparent lack of cross polarization. The predicted short Rayleigh length at $\omega_0 = 4$ mm was observed, and inspection of Fig. 8(b) confirms the focused beam waist is located prior to the surface of the cornea. The nearly Gaussian field distribution was attributed to the negligible effect of reflector geometry, as the local curvature of the OAP segment, subtended by a 4-mm-radius beam, for large R_s, was nearly symmetric about the beam centroid.

A complementary example of a large input beam radius ($\omega_0 = 12$ mm) paired with a short scan radius ($R_s = 24.7$ mm) is displayed in Fig. 8(f)–(h). The increased beam radius and mirror curvature result in the focused beam waist lying nearly coincident with the corneal CoC/OAP focal point, which is visible in the $x'z'$ cut in Fig. 8(g). Increased diffraction and the effects of increased mirror asymmetry about the beam centroid are also apparent and manifest as multiple local extremum in the field distributions of Fig. 8(g) and (h) and significant radial asymmetry in Fig. 8(h).

The average spot size on target ($x'y'$ tangent plane) was computed numerically by obtaining the modulus of the E-field, finding the location of the peak amplitude, computing the 1/*e* closed contour of the modulus, and then computing the average radius of the 1/*e* contour. These results are superimposed with a square marker (□) in Fig. 7(a) and demonstrate good agreement between quasi-optical analysis and physical optics. The level of fit is further explored in Fig. 7(b), which reports the difference between quasi-optical radius $(\omega_{1,q})$ and physical optics average radius $(\omega_{1,p})$: $\omega_{1,q} - \omega_{1,p}$. The spot size differential further substantiates the general correlation between decreasing spot size radius and improved goodness of fit. Additionally, the graph elucidates the increased effects of diffraction and offset reflector configuration for larger input radii (ω_0) and smaller scan radii (R_s).

B. Coupling

The electric field of the input and return beams at the reference plane were sampled for every pair of ω_0 and R_s. The magnitude of the reflected beam for the $\omega_0 = 4$ mm, $R_\mathrm{s} = 76.9$ mm pair demonstrates a significant increase in main lobe extent compared to the initial 4 mm. This corroborates with the results obtained with quasi-optical analysis that indicate substantial beam divergence over the optical path, which manifests in a broad recollimated beam radius [see Fig. 8(c) and (h)]. Additionally, the multiple extremum in the wrapped phase plot [see Fig. 8(e) and (j)] suggests that the reference plane is located approximately one Rayleigh length from the mirror surface corroborating a curved phased front and thus appreciable beam divergence.

The converse is true for the $\omega_0 = 12$ mm, $R = 24.7$ mm beam, which demonstrates a transverse extent at the reference plane only slight larger than the initial beam. The phase plot is also more uniform with extrema spaced farther apart. These plots indicate that the reference plane is likely well within one collimated beam Rayleigh length and strongly corroborate with the quasi-optical analysis

$$\bar{K}_3 = \frac{\left| \iint \vec{E}_\mathrm{inc} \cdot \vec{E}_\mathrm{ref} \right) dA \Big|^2}{\iint \left| \vec{E}_\mathrm{inc} \right|^2 dA \iint \left| \vec{E}_\mathrm{ref} \right|^2 dA}, \quad \text{where} \begin{cases} \vec{E}_\mathrm{inc} = \vec{E}_0 \\ \vec{E}_\mathrm{ref} = \vec{E}_3. \end{cases} \tag{17}$$

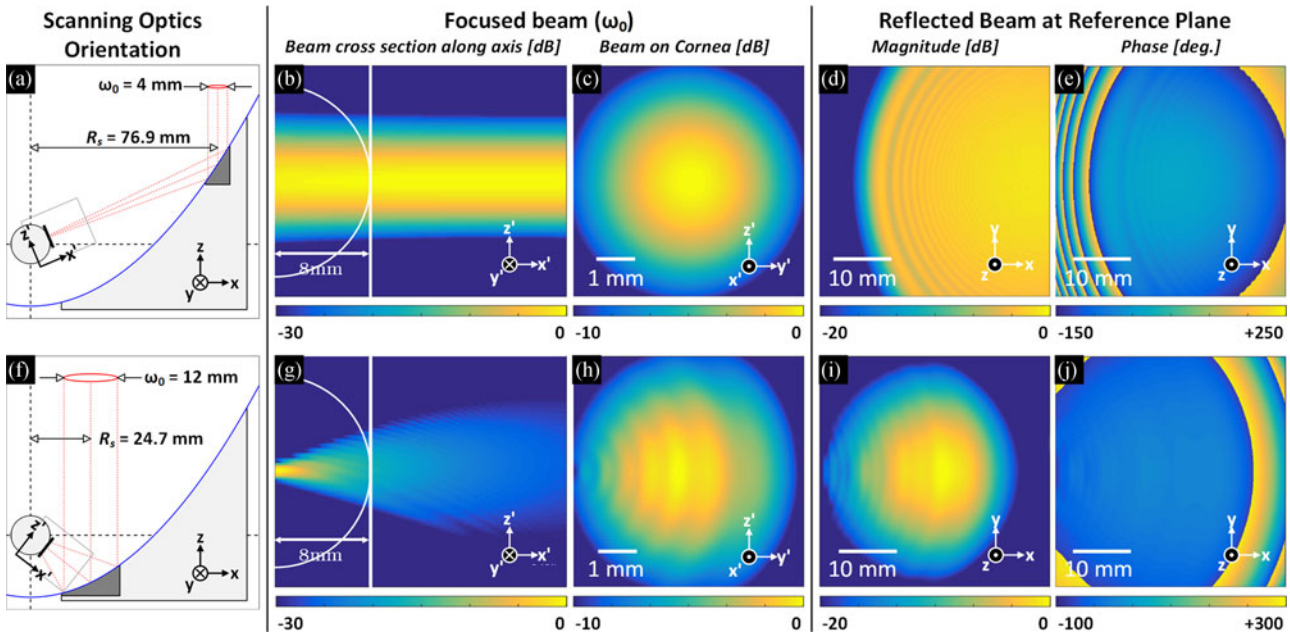

Fig. 8. (a) Layout for $\omega_0 = 4$ mm and $R = 76.9$ mm. (b) Cross section of beam in the $x'z'$ plane. (c) Beam profile on the $y'z'$ plane tangent to the cornea and coincident with the intersection of the focused beam centroid and corneal surface. Electric field magnitude (d) and phase (e) of the beam at the reference plane (xy plane) following reflection from the cornea and recollimation from the OAP. (f) Layout for $\omega_0 = 12$ mm and $R = 24.7$ mm. (g)–(j) are same as (b)–(e). Note that in configuration (a), the fields are nearly Gaussian, while in configuration (f), they are not due to the offset reflector configuration and possible diffraction. Blue corresponds to lower E-field amplitude and yellow corresponds to higher.

The coefficient quantifies the field correlation between the incident electric field at the input beam plane, $\vec{E}_{\text{inc}}$, and the field reflected from the cornea through the OAP up to the same input plane, $\vec{E}_{\text{ref}}$. This coefficient was computed with (17), which references the square of the inner product of the vector fields with the product of the total energy in each field. The complex vector inner product accounts for mismatch between amplitude, phase, and polarization. The coupling coefficient computations were superimposed with a square marker (□) in Fig. 7(b) and again demonstrate good agreement between quasi-topical methods and physical optics. The differential between the quasi-optical coupling coefficient ($K_{3,\text{p}}$) and the physical optics coupling coefficient ($K_{3,q}$), i.e., $K_{3,p} - K_{3,q}$, is plotted in Fig. 7(d) and reveals a maximum deviation of ∼6.5% at ω_0 ∼8 mm and R ∼76.9 mm. The differentials for larger input beam radii are not monotonic across the scan range, and this variation is likely the result of edge diffraction and cross polarization.

VII. Beam Radius Optimization

Inspection of Fig. 7(a) and the tradeoffs listed in Section V-B motivate the optimization of input spot size subject to a specific resolution criterion. Two candidate metrics were considered in the following equations, where ω_0 is the input collimated beam radius and ω_1 is the focused beam radius on the cornea. $R_{s,1} = 2f_0 - A/2 + \omega_0$ is the "unclipped" scan radius corresponding to the near edge of the OAP, and $R_{s,2} = 2f_0 + A/2 - \omega_0$ is the "unclipped" scan radius corresponding to the far edge of the OAP mirror as follows:

$$\omega_0 \text{ s.t. } \omega_1\left(R_{s,1}, \omega_0\right) - \omega_1\left(R_{s,2}, \omega_0\right) = 0 \tag{18}$$

$$\omega_0 \text{ s.t. } \frac{\partial}{\partial \omega_0}\left(\frac{1}{R_{s,2} - R_{s,1}} \int_{R_{s,1}}^{R_{s,2}} \omega_1\left(r,\, \omega_0\right) dr\right) = 0. \tag{19}$$

Equation (18) chooses input beam diameter ω_0 such that the resulting spot sizes on the target at the extremums of the scan range $[R_{s,1},\ R_{s,2}]$ are equal. The solution to (18) corresponds to an approximate colocation of the smallest focused spot size with the apex of the cornea, while trying to minimize the asymmetry of the spot size about the corneal apex. Equation (19) chooses a collimated beam radius, where the average focused spot size at the corneal surface is minimized. The parameter space and solutions to these equations are displayed in Fig. 9 using the quasi-optical along with physical optics results of Fig. 7(a). The crossover point of the two curves that satisfy (18) is denoted with the gray circle (○) marker and occurs at a collimated input waist of 6.25 mm.

The input-spot-size-dependent behavior of the solution of the differential in (19) is denoted with the solid black line in Fig. 9, and its minimum, which satisfies (19), is denoted by the circular marker (○) at $\omega_0 = 7.6$ mm. The physical-optics-derived solution is plotted with the square (□) marker. The results demonstrated good agreement and identified an optimal input radius of ω_0 ∼7.0 mm.

For current clinical practice, the corneal center provides most utility when identifying disease processes, thus justifying the metric in (18) [37]. However, certain corneal pathologies, e.g., corneal graft rejection, can create "edematous fronts" that can start from anywhere in the periphery and migrate across the

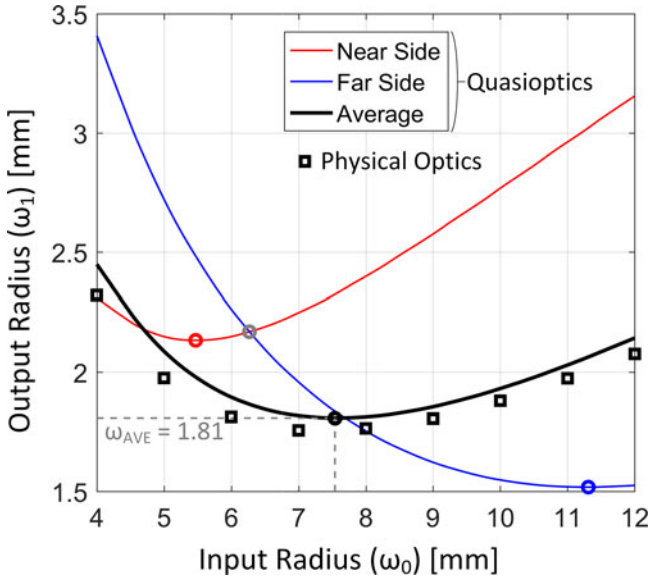

Fig. 9. Optimization space for (18) and (19). The intersection of the near (red) and far (blue) edge traces is the solution to (18). The black curve represents the argument of the derivative in (19) and the black circular (○) marker is the solution of (19). The square (□) markers were computed from the physical optics simulations.

extent of the corneal surface [4]. Detection of these features supports minimizing the spatial bias of imaging system, thus justifying the metric in (19). Note that with the optimized $\omega_0 = 7.6$ mm, the focused beam waist is never coincident with the corneal surface.

VIII. Experimental Validation of Optical Theory

A prototype system was assembled to explore the accuracy of the quasi-optical theory and physical optics simulations. The coupling coefficient was chosen as a representative test because it is dependent on four parameters: input radius of curvature, output radius of curvature, input beam radius, and output beam radius.

The matching between theoretical and experimental coupling coefficient was explored by imaging a 7.93-mm-radius brass sphere. Given the lack of contrast in the target, any spatial variation in signal was attributed to the predicted spatially varying coupling efficiency.

A. System

A prototype system, based on the optics of Fig. 5, was constructed with a solid-state frequency-modulated continuous wave THz source (Amplifier–multiplier chain, Virginia Diodes, Virginia) centered at 650 GHz. The detector was a WR1.5 waveguide mounted Schottky diode detector (ZBD) (Virginia Diodes, VA) with a 500–700-GHz detection bandwidth. Both the source and detector were coupled to diagonal feedhorn antennas with 26 dB of gain and aperture dimensions of 2.4 mm × 2.4 mm. To mitigate standing waves, the output was frequency modulated over ∼2 GHz at a rate of 100 kHz, producing an RF bandwidth that exceeded the expected full etalon period of the optical path.

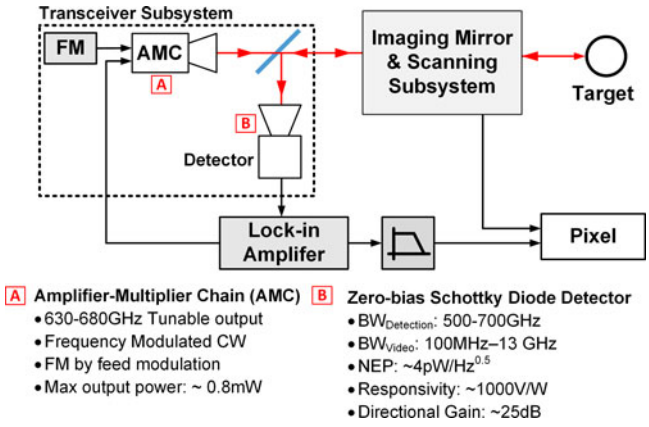

Fig. 10. Block diagram of the prototype system.

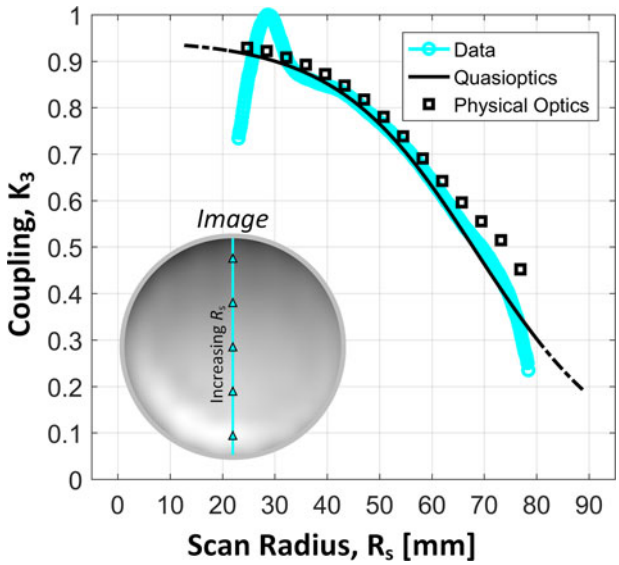

Fig. 11. Coupling calibration target with data fit to (15).

The source was also amplitude modulated at ∼900 Hz, and the rectified signal from the ZBD was detected with a Lock-in amplifier (Stanford Research Systems, CA) using an integration time of 3 ms. These parameters are summarized in the block diagram of Fig. 10.

The optical layout of the system (see Fig. 5) used 25.4-mm PFL, 76.2-mm CA, 90° OAP mirrors to collimate radiation from the multiplier chain and focus reflected radiation into the detector aperture. The combination of feedhorn directivity and OAP PFL yielded a collimated spot 1/*e* field radius of ∼10 mm as measured with a knife edge target. The imaging mirror was a 76.2-mm CA, 25.4-mm PFL OAP. Beam scanning was performed with two 50.8-mm-diameter gold coated plane mirrors.

B. Image and Coupling Coefficient Fits

A THz image of the brass sphere is displayed in the inset of Fig. 11 and was acquired by translating the plane mirrors with 5-mm steps. Note that these data are a mapping of the

reflectivity on the sphere to the transverse coordinates of the CA, and thus, the data were directly compared to the simulation results in Figs. 7 and 8. The image was masked with a circle of radius $A/2 - \omega_0$ to exclude aberrations due to beam clipping.

The inset image in Fig. 11 shows a general trend of decreasing signal starting from the near edge of the mirror aperture and continuing, monotonically, to the far edge (decreasing signal for increasing scan radius). A localized increase in signal is apparent in the bottom left corner of the image, which is likely due to beam diffraction. A contour line was superimposed on the aperture diameter. The arrows on the contour line correspond to increasing scan radius, and the pixels sampled by this profile are plotted with a circular line style (○) in Fig. 11.

The quasi-optical [see (15)] and physical optics simulations for an input beam radius of 10 mm are superimposed on the data in a solid line style (–) and square marker (□), respectively (obtained directly from Fig. 7). The experimental data and simulation results demonstrate good agreement across the center of the masked aperture of the mirror. The minimum deviation occurs at the mirror center ($R_s = 50.8$ mm), while the maximum deviation occurs toward the mirror near edge ($R_s = 28$ mm). This indicates that diffraction may contribute to observed contrast beyond $\mathrm{A}/2 - \omega_0$ and support the exploration of smaller mask radii.

IX. Conclusion

This work presents a novel imaging principle and analysis method for normal incidence noncontact THz imaging of spherical targets with applications to corneal diagnostics. An analysis of the variation in the geometric properties of the cornea was presented. It was shown that when referenced to a THz wavelength, the cornea can be considered an ideal sphere, even under perturbations from corneal diseases and the effects of surgical interventions. This analysis motivated the design of a corneal imaging system that places the corneal CoC coincident with the focal point of a low *f*/# OAP mirror. Transverse sweeping of a collimated beam in the CA plane produces angular scanning of a focused beam along the surface of the cornea.

Quasi-optical techniques were introduced that segment parabolic mirrors into an ensemble of thin lenses, where the EFL and free-space beam paths are proportional to the distance between the parent focal point and mirror CA centroid. The spot size on target, radius of curvature pre- and postreflection, and coupling coefficient between transmit and received beams were simulated for a single OAP reflector.

The spot size on target and quasi-optical coupling coefficient were also computed with full-wave physical optics, and good agreement between the physical optics results and the quasi-optical results was demonstrated. The imaging mirror was over dimensioned ($A >> \omega_0$); therefore, diffractive effects were limited for most of the considered input parameter space. The concurrence of the results strongly supports the use of quasi-optical techniques as a design and analysis tool.

An imaging system based on Fig. 5 was constructed and used to acquire images of a brass ball target with an RoC matching that of cornea. A profile of intensity variation along the vertical diameter of the image was compared with the quasi-optical and physical optics theory, and good agreement was observed between image contrast and predicted coupling coefficients.

The limited variation of the shape and size of cornea among adult population is unique among all structures in the body and, when referenced to the typical center wavelength of a THz imaging system, even more negligible. We believe that the presented systems and analysis techniques provide a good first step toward the *in vivo* translation of this technology to human subjects.

Acknowledgment

The authors would like to thank L. Han at Taylor and Francis for facilitating the discussions that lead to this research.

References

[1] A. P. Adamis, V. Filatov, B. J. Tripathi, and R. A. M. C. Tripathi, "Spotlight on exhibitors Fuchs' endothelial dystrophy of the cornea," *Survey Ophthalmol.*, vol. 38, pp. 149–168, Sep. 1, 1993.

[2] Y. S. Rabinowitz, "Keratoconus," *Survey Ophthalmol.*, vol. 42, pp. 297–319, Jan. 1998.

[3] D. M. Taylor, B. F. Atlas, K. G. Romanchuk, and A. L. Stern, "Pseudophakic bullous keratopathy," *Ophthalmology*, vol. 90, pp. 19–24, Jan. 1983.

[4] A. Panda, M. Vanathi, A. Kumar, Y. Dash, and S. Priya, "Corneal graft rejection," *Survey Ophthalmol.*, vol. 52, pp. 375–396, Jul. 2007.

[5] J. P. Whitcher, M. Srinivasan, and M. P. Upadhyay, "Corneal blindness: A global perspective," *Bull. World Health Org.*, vol. 79, pp. 214–221, 2001.

[6] G. O. Waring, III, R. Stulting, and D. Street, "Penetrating keratoplasty for pseudophakic corneal edema with exchange of intraocular lenses," *Arch. Ophthalmol.*, vol. 105, pp. 58–62, 1987.

[7] J. Ytteborg and C. H. Dohlman, "Corneal edema and intraocular pressure: II. Clinical results," *Arch. Ophthalmol.*, vol. 74, pp. 477–484, 1965.

[8] G. O. Waring, M. M. Rodrigues, and P. R. Laibson, "Corneal dystrophies. II. Endothelial dystrophies," *Survey Ophthalmol.*, vol. 23, pp. 147–168, Nov. 1, 1978.

[9] M. M. Rodrigues, J. H. Krachmer, J. Hackett, R. Gaskins, and A. Halkias, "Fuchs' corneal dystrophy," *Ophthalmology*, vol. 93, pp. 789–796, Jun. 1, 1986.

[10] J. H. Krachmer, J. J. Purcell, Jr., C. W. Young, and K. D. Bucher, "Corneal endothelial dystrophy: A study of 64 families," *Arch. Ophthalmol.*, vol. 96, pp. 2036–2039, 1978.

[11] Z. D. Taylor *et al.*, "THz and mm-Wave sensing of corneal tissue water content: In vivo sensing and imaging results," *IEEE Trans. THz Sci. Technol.*, vol. 5, no. 2, pp. 184–196, Mar. 2015.

[12] Z. D. Taylor *et al.*, "THz and mm-wave sensing of corneal tissue water content: Electromagnetic modeling and analysis," *IEEE Trans. THz Sci. Technol.*, vol. 5, no. 2, pp. 170–183, Mar. 2015.

[13] D. B. Bennett *et al.*, "Terahertz sensing in corneal tissues," *J. Biomed. Opt.*, vol. 16, 2011, Art. no. 057003.

[14] Z. Liu, A. J. Huang, and S. C. Pflugfelder, "Evaluation of corneal thickness and topography in normal eyes using the Orbscan corneal topography system," *Brit. J. Ophthalmol.*, vol. 83, pp. 774–778, 1999.

[15] Y. Li, R. Shekhar, and D. Huang, "Corneal pachymetry mapping with high-speed optical coherence tomography," *Ophthalmology*, vol. 113, pp. 792–799, May 2006.

[16] A. Gullstrand, "Appendix," in *Handbuch der physiologischen Optik*, vol. 1, H. V. Helmholtz, Ed. New York, NY, USA: Dover, pp. 351–352.

[17] S. Srivannaboon, D. Z. Reinstein, H. F. S. Sutton, and S. P. Holland, "Accuracy of Orbscan total optical power maps in detecting refractive change after myopic laser in situ keratomileusis," *J. Cataract Refractive Surgery*, vol. 25, pp. 1596–1599, Dec. 1999.

[18] S. J. Bogan, G. O. Waring, III, O. Ibrahim, C. Drews, and L. Curtis, "Classification of normal corneal topography based on computer-assisted videokeratography," *Arch. Ophthalmol.*, vol. 108, pp. 945–949, 1990.

[19] O. Hockwin, E. Weigelin, H. Laser, and V. Dragomirescu, "Biometry of the anterior eye segment by Scheimpflug photography," *Ophthalmic Res.*, vol. 15, pp. 102–108, 1983.

[20] R. A. Applegate and H. C. Howland, "Noninvasive measurement of corneal topography," *IEEE Eng. Med. Biol. Mag.*, vol. 14, no. 1, pp. 30–42, Jan./Feb. 1995.

[21] J. Schwiegerling and J. E. Greivenkamp, "Using corneal height maps and polynomial decomposition to determine corneal aberrations," *Optometry Vision Sci.*, vol. 74, pp. 906–916, 1997.
[22] J. Ø. Hjortdal, L. Erdmann, and T. Bek, "Fourier analysis of video-keratographic data. A tool for separation of spherical, regular astigmatic and irregular astigmatic corneal power components," *Ophthalmic Physiol. Opt.*, vol. 15, pp. 171–185, 1995.
[23] T. W. Raasch, "Corneal topography and irregular astigmatism," *Optometry Vision Sci.*, vol. 72, pp. 809–815, 1995.
[24] J. H. Krachmer, R. S. Feder, and M. W. Belin, "Keratoconus and related noninflammatory corneal thinning disorders," *Survey Ophthalmol.*, vol. 28, pp. 293–322, Jan. 1984.
[25] S. J. Gromacki and J. T. Barr, "Central and peripheral corneal thickness in keratoconus and normal patient groups," *Optometry Vision Sci.*, vol. 71, pp. 437–441, 1994.
[26] L. P. Lee, "The transverse mercator projection of the entire spheroid," *Empire Survey Rev.*, vol. 16, pp. 208–217, Jan. 1, 1962.
[27] J. P. Snyder, "Map projections used by the U.S. geological survey, USGS numbered series," U.S. Govt. Printing Office, Washington, DC, USA, Rep. 1532, 1982.
[28] P. Goldsmith, *Gaussian Beam Quasioptical Propogation and Applications*. Piscataway, NJ, USA: IEEE Press, 1998.
[29] J. A. Murphy, "Distortion of a simple Gaussian beam on reflection from off-axis ellipsoidal mirrors," *Int. J. Infrared Millimeter Waves*, vol. 8, pp. 1165–1187, Sep. 1, 1987.
[30] R. M. Malone *et al.*, "Design of a thermal imaging diagnostic using 90-degree off-axis parabolic mirrors," *Proc. SPIE*, vol. 6288, 2006, Art. no. 62880Z.
[31] E. Zauderer, "Complex argument Hermite–Gaussian and Laguerre–Gaussian beams," *J. Opt. Soc. Amer. A*, vol. 3, pp. 465–469, 1986.
[32] A. E. Siegman, "Hermite–Gaussian functions of complex argument as optical-beam eigenfunctions," *J. Opt. Soc. Amer.*, vol. 63, pp. 1093–1094, 1973.
[33] F. Pampaloni and J. Enderlein, "Gaussian, Hermite-Gaussian, and Laguerre-Gaussian beams: A primer," *arXiv preprint physics/0410021*, 2004.
[34] N. Llombart, K. B. Cooper, R. J. Dengler, T. Bryllert, and P. H. Siegel, "Confocal ellipsoidal reflector system for a mechanically scanned active terahertz imager," *IEEE Trans. Antennas Propag.*, vol. 58, no. 6, pp. 1834–1841, Jun. 2010.
[35] K. B. Cooper *et al.*, "An approach for sub-second imaging of concealed objects using terahertz (THz) radar," *J. Infrared, Millimeter, Terahertz Waves*, vol. 30, pp. 1297–1307, 2009.
[36] K. B. Cooper *et al.*, "THz imaging radar for standoff personnel screening," *IEEE Tran. THz Sci. Technol.*, vol. 1, no. 1, pp. 169–182, Sep. 2011.
[37] B. Lackner, G. Schmidinger, S. Pieh, M. A. Funovics, and C. Skorpik, "Repeatability and reproducibility of central corneal thickness measurement with pentacam, orbscan, and ultrasound," *Optometry Vision Sci.*, vol. 82, pp. 892–899, 2005.